Optics & Laser Technology 179 (2024) 111394

Contents lists available at ScienceDirect

Optics and Laser Technology

journal homepage: www.elsevier.com/locate/optlastec

Full length article

Compact Q-switched vortex waveguide laser modulated by buried Ag nanoparticles in SiO_2

Wenqing Sun [a], Fengqin Liu [a], Jing Guan [a], Carolina Romero [b], Javier R. Vázquez de Aldana [b], Feng Ren [c], Yuechen Jia [a], Xiaoli Sun [a,*], Feng Chen [a,*]

[a] School of Physics, State Key Laboratory of Crystal Materials, Shandong University, Jinan 250100, China
[b] Grupo de investigación en Aplicaciones de0l Lásery Fotónica, Universidad de Salamanca, Salamanca 37008, Spain
[c] Department of Physics, Center for Ion Beam Application and Center for Electron Microscopy, Wuhan University, Wuhan 430072, China

ARTICLE INFO

Keywords:
Plasmonic nanoparticles
Localized surface plasmon resonance effect
Nonlinear optical response
Nd:YAG waveguide
Q-switched vortex laser

ABSTRACT

Vortex beam, particularly pulsed vortex laser, has expanded the potential applications in optics due to their unique wave-front phase structure and the determined photon orbital angular momentum. In this study, we present a novel approach including the integration of fused silica embedded with silver nanoparticles (Ag:SiO_2) into the Nd:YAG waveguide platform for achieving nanosecond vortex pulses. Using a spiral phase plate for in-cavity phase modulation, we successfully demonstrate a Q-switched vortex laser with a high repetition rate in the megahertz range and short pulse width in the nanosecond regime. Additionally, we conduct a comprehensive analysis of the near-field distributions of Ag nanoparticles with varying sizes and distributions using COMSOL simulation. This study exemplifies the integration of silica-based photonic elements for realizing a high-stability and cost-effective nanosecond vortex laser system.

1. Introduction

Vortex beam, carrying the orbital angular momentum (OAM) of $l\hbar$ per photon [1], plays an irreplaceable role in various applications [2–4], such as optical tweezer manipulation [5–7], optical communication [8,9], quantum information storage and quantum cryptography [10,11]. Additionally, vortex beams offer promising applications in material machining [12,13], microscopy and imaging [14–16], strong-field physics [17]. To date, researchers have successfully realized continuous-wave (CW) vortex beams by incorporating various modulation elements into the resonator [18–23]. It is worth noting that pulsed vortex lasers exhibit excellent performance in optical processing due to high peak power and repetition frequency [13,24]. The interaction between vortex pulses with particles leads to nonlinear effects, making them indispensable in microscopic particle manipulation [25,26]. Hence, pulsed vortex lasers play an increasingly important role in various application fields, and the generation of pulsed vortex lasers has attracted much attention [27–30].

It is well known that pulsed lasers are typically realized by mode-locked and Q-switched operations, and the saturable absorber (SA) plays a crucial role [31]. In contrast to conventional semiconductor saturable absorber mirrors, novel two-dimensional (2D) materials featuring narrow bandgaps and strong light-matter interactions have proven effective as saturable absorbers [32–34], enabling the realization of pulsed laser. While, the 2D materials are prone to oxidation when exposed to air for extended periods, which hinders the improvement of the stability of lasers. Recently, noble metallic nanoparticles (NPs) attracted renewed interest in the field of pulsed laser generation and researchers have successfully modulated the nonlinear response of dielectric materials by incorporating the embedded noble metallic NPs within them [35–37]. The main mechanism is the localized surface plasmon resonance (LSPR) effect, which occurs due to the interaction between the incident photoelectric field and the metallic NPs [38–40].

Optical waveguides play a fundamental role in integrated photonics systems [41,42]. The waveguide structure provides strong optical confinement, leading to a significant increase in optical intensity within the waveguide geometry while maintaining the original optical performance of the bulk material [43]. Cladding waveguides, which can be integrated with standard fibers, are capable of supporting single-mode guidance and are particularly suitable for high-power lasers with high beam quality, especially in Q-switched and mode-locked operations [44]. Various methods have been employed for cladding waveguide

* Corresponding authors.
E-mail addresses: xlsun@sdu.edu.cn (X. Sun), drfchen@sdu.edu.cn (F. Chen).

https://doi.org/10.1016/j.optlastec.2024.111394
Received 31 March 2024; Received in revised form 22 May 2024; Accepted 26 June 2024
Available online 29 June 2024

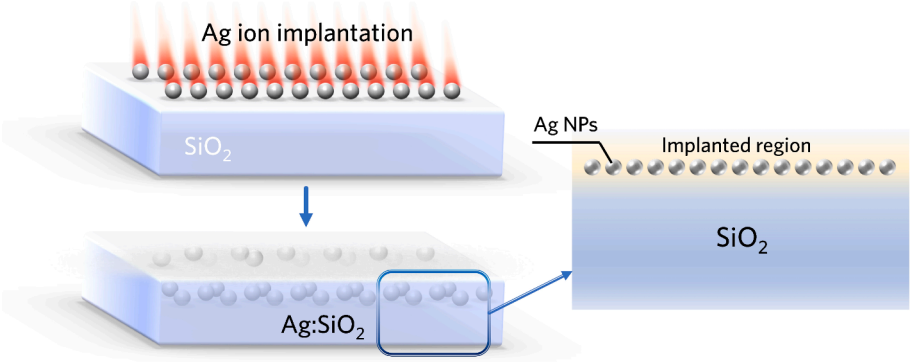

Fig. 1. Schematic diagram of the Ag:SiO_2 system formed by implanting Ag NPs into SiO_2. Inset: schematic diagram of Ag:SiO_2 cross-section.

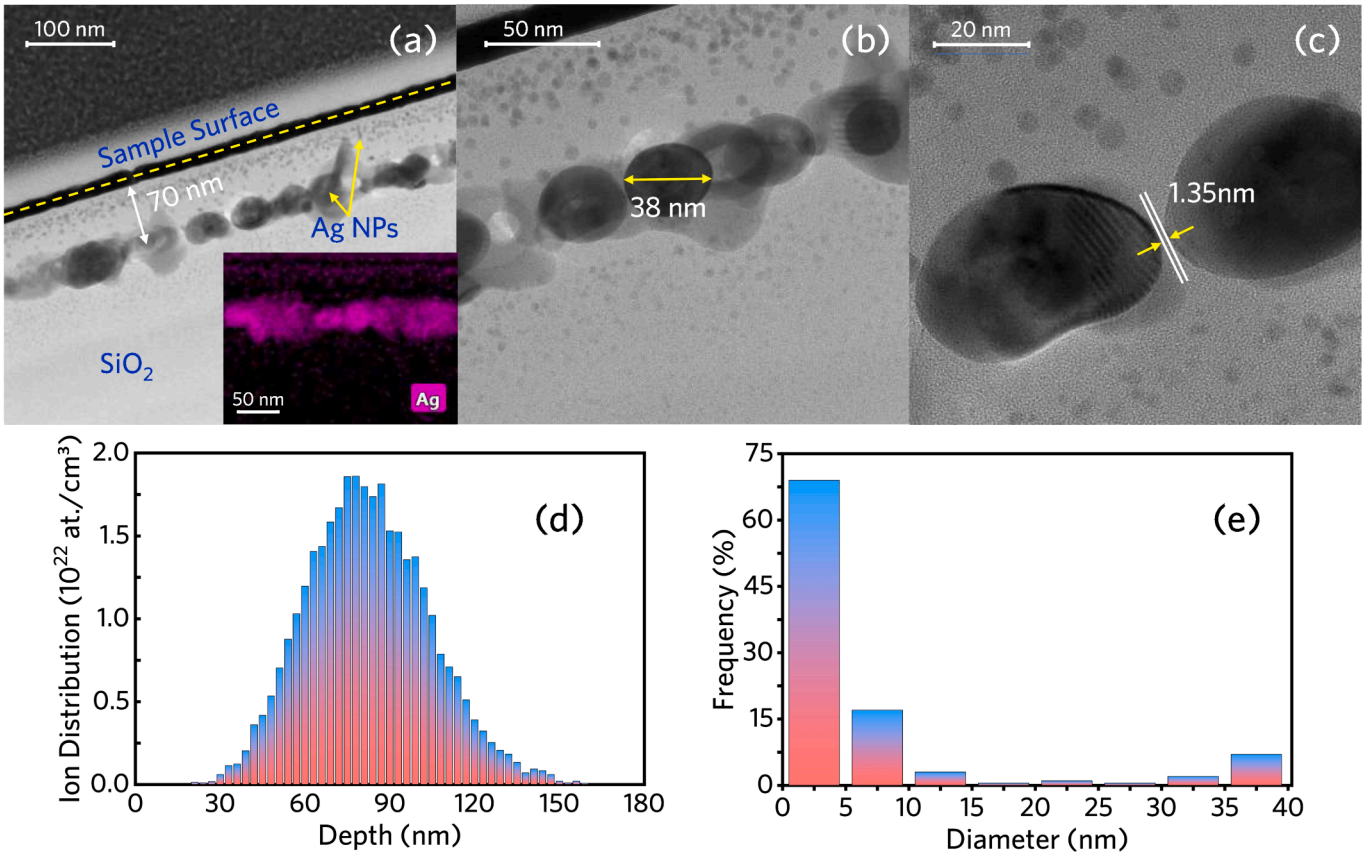

Fig. 2. Morphology and distribution characterization of NPs. (a) Cross-sectional TEM of Ag:SiO_2 in the near surface region. The element mapping image is shown as inset. (b) TEM image of the distribution of NPs. (c) HRTEM image of the NPs. (d) The ion distribution of Ag^+ ions implanted SiO_2 calculated by SRIM. (e) The size distribution of Ag NPs based on TEM image.

fabrication, including ion/proton exchange, ion-beam implantation/irradiation, and femtosecond laser direct writing (FsLDW) technology. Among these techniques, FsLDW creates tracks within the YAG crystal with reduced refractive index. The waveguide core is usually encircled by multiple tracks, forming Type II and Type III configuration waveguides. Therefore, the ultrafast laser writing is a powerful and promising method to fabricate optical waveguides with diverse geometries [43,45].

In this study, we demonstrate that the integration of SiO_2 with Ag NPs can be used as a saturable absorber for achieving a nanosecond vortex laser in Nd:YAG cladding waveguide with "ear-like" structure. The linear absorption response of Ag:SiO_2 is measured experimentally and simulated. By open-aperture Z-scan method, Ag:SiO_2 shows an obvious saturation absorption behavior in the near-infrared region, which can be attributed to the LSPR of the encapsulated Ag NPs. Based on Ag:SiO_2 SA, a Q-switched vortex laser with a repetition rate of 6.824 MHz and a pulse width of 28 ns on Nd:YAG waveguide platform. This work marks a major breakthrough in developing the utilization of silicon-based photonic devices in Q-switched laser systems, presenting fresh opportunities for achieving cost-effective and high stable Q-switched vortex laser systems.

2. Ag:SiO_2 sample characterization

The process of fabricating the Ag:SiO_2 system is illustrated in Fig. 1. Ag ions are injected into SiO_2 using an ion implanter (LC22-IC0-01) with an energy of 160 keV and ion fluence of 1×10^{17} ions/cm^2, resulting in the formation of NPs when the concentration of metal atomic monomer

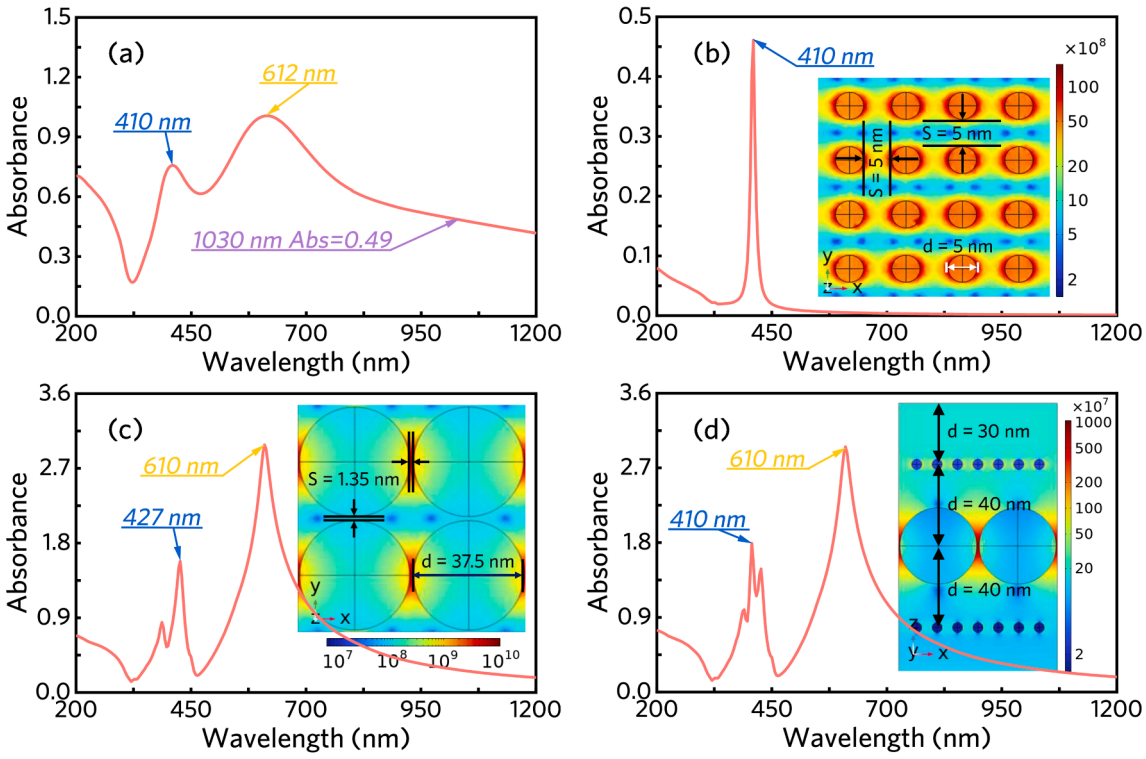

Fig. 3. Characterization of linear optical absorption. (a) Experimental linear absorption spectra of Ag:SiO_2. (b) Simulated linear absorption spectra of Ag:SiO_2 based on small-sized Ag NPs array model. Inset shows the electric field distribution of small-sized NPs under excitation of the laser with the wavelength of 410 nm. (c) Simulated linear absorption spectra of Ag:SiO_2 based on large-sized Ag NPs array model. Inset shows the electric field distribution of large-sized NPs under excitation of the laser with the wavelength of 610 nm. (d) Simulated linear absorption spectra of Ag:SiO_2 based on both large and small-sized Ag NPs array models. Inset shows the electric field distribution of the NPs under excitation of the laser with the wavelength of 1030 nm.

exceeds the solid solubility threshold of the dielectric material. This leads to the assembly of SiO_2 encapsulated with Ag NPs. Cross-section schematic diagram of Ag:SiO_2 is depicted in Fig. 1. The morphology and distribution of Ag NPs are characterized by TEM (Talos F200X), as presented in Fig. 2(a)-(c). It can be clearly seen from Fig. 2(a) that the implanted Ag^+ ions spontaneously aggregate to form the Ag NPs. The Ag element mapping image, shown in the inset of Fig. 2(a), further confirms the formation of Ag NPs. The average depth of the NPs layer is 70 nm, which is consistent with the calculated results (Fig. 2(d)) by the Stopping and Range of Ions in Matter (SRIM 2013). As shown in Fig. 2(b), the size of large-sized NPs layer is roughly between 35 nm-40 nm. In addition, there are discrete small-sized NPs distributed near the large-sized NPs layer and the surface. The corresponding statistical information of NPs size extracted from TEM is displayed in Fig. 2(e). The NPs with diameters ranging from 0 to 5 nm are the most abundant, accounting for 69% of the total NPs. Fig. 2(c) shows that the morphology of NPs is near-spherical. And it is worth noting that due to the high NPs volume fraction, the spacing between large-sized NPs is very small, roughly 1.35 nm.

The experimentally measured optical absorbance spectra of Ag:SiO_2 is presented in Fig. 3(a). A typical LSPR absorption peak at 410 nm is clearly characterized, which is consistent with previous report [46–48]. Besides, an additional atypical LSPR main absorption peak at 612 nm is also observed. At 1030 nm, the absorbance is about 0.49. However, in the previous report, typical absorption peak almost has no response at all in the near infrared. To investigate the reasons for the near-infrared response of NPs, we constructed the three NPs models to explore their absorption spectra from a theoretical simulation. The first nanocrystal model, as shown in the inset of Fig. 3(b), consists of NPs with a diameter of 5 nm and a spacing of 5 nm. From the simulation results, it can be seen that the LSPR absorption peak of Model 1 is located at 410 nm, with a

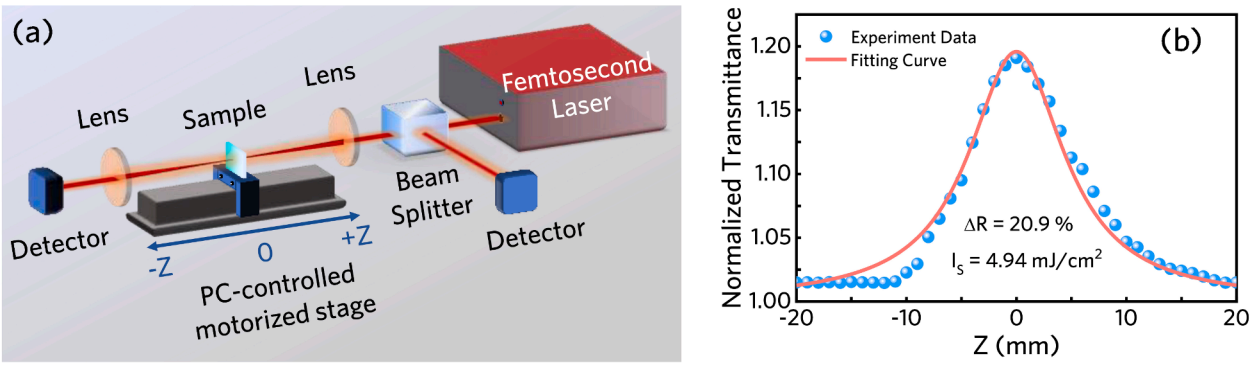

Fig. 4. Femtosecond open-aperture Z-scan characterization of Ag:SiO_2. (a) Schematic diagram of the femtosecond open-aperture Z-scan experiment setup. (b) Open-aperture Z-scan results of Ag:SiO_2 under the irradiation of femtosecond laser with 340 fs at 1030 nm.

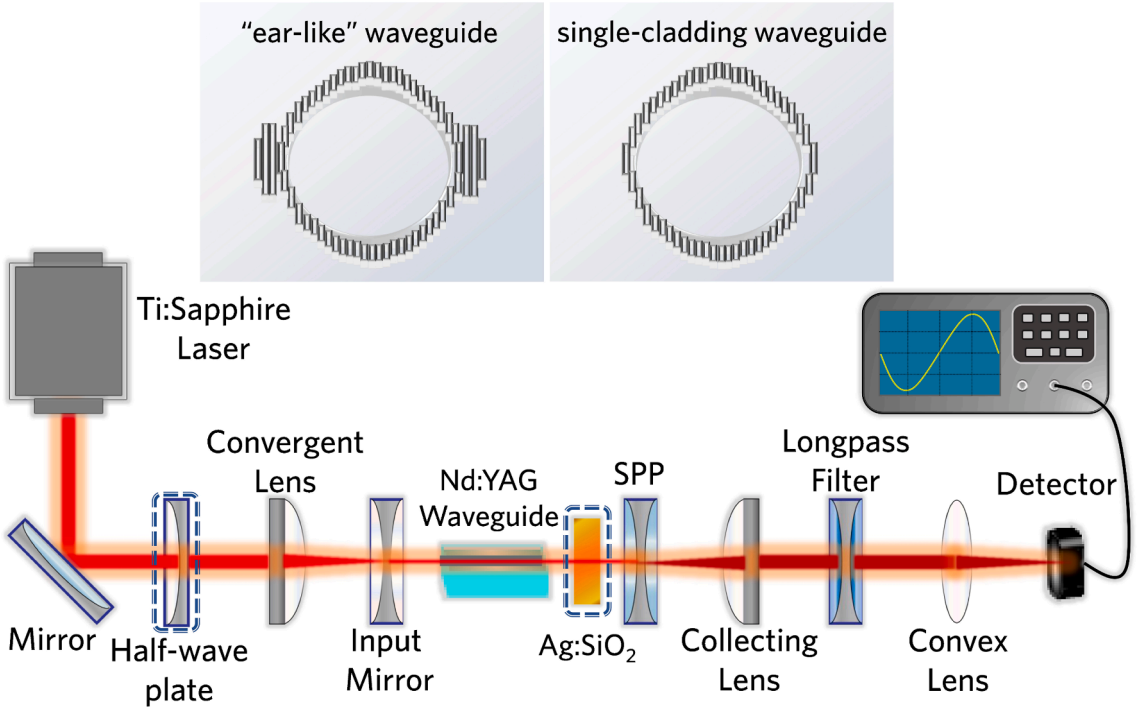

Fig. 5. Schematic diagram of the Q-switched vortex laser experiment setup. Inset: schematic diagrams of "ear-like" waveguide and single-cladding waveguide.

narrow absorption peak width, which is in consistent with previous reports [35,49]. The second model, as shown in the inset of Fig. 3(c), has larger nanoparticle diameter of 37.5 nm and closer spacing of 1.35 nm. In Fig. 3(c), it can be observed that not only does the typical characteristic peak undergo a redshift, but also a new atypical characteristic absorption peak appears at 610 nm. This is attributed to the smaller spacing between the NPs, resulting in stronger coupling between them. Interestingly, the full width at half maximum of the atypical absorption peak has significantly widened, thereby broadening the LSPR response bandwidth of the NPs to the near-infrared range. From TEM (Fig. 2), it can be seen that the size of NPs near the surface is smaller. About 70 nm away from the surface, there is a layer of large-sized NPs. In deeper regions away from the surface, the NPs are smaller in size and more sparsely distributed. Thus, according to the NPs distribution extracted from TEM, the third model is conducted, as shown in the inset of Fig. 3 (d). Although the model simplifies the distribution of small-sized NPs, it does not affect the accuracy of the simulation results. It can be seen that the simulation results are in good agreement with the experimental results (Fig. 3(a)). At 1030 nm, the theoretical absorbance is 0.25, slightly lower than the experimental measurement, which may due to the increased effective optical path length induced by nanoparticle scattering, thereby enhancing light absorption. Through experimental and simulation results, it has been successfully demonstrated that the prepared Ag:SiO_2 exhibits strong light absorption capability in the near-infrared range, and is expected to become a nonlinear optical modulation device.

The experimental data and simulation results of linear optical absorption of Ag:SiO_2 show that the LSPR response at near-infrared region is significantly enhanced by the unconventional peak due to the complex synergistic effect. Hence, further investigation is required to explore the nonlinear optical response of Ag:SiO_2, particularly focusing on its saturation absorption characteristics. As shown in Fig. 4(a), an open-aperture Z-scan system with the excitation laser of 340 fs, 25 kHz, 1030 nm is employed. The experimental results of the normalized transmittances as function of the sample position along the Z-axis is depicted in Fig. 4(b). The shape of the narrow peak appearing at the focal point (z = 0) is highly symmetrical, confirming that Ag:SiO_2 possesses the valid typical saturable absorption property. In order to quantitatively characterize the nonlinear optical response, the saturation intensity of 4.94 mJ/cm^2 and the modulation depth of 20.9% are obtained by nonlinear fitting of the experimental data. The fitting model formula is as follows:

$$T = \left(1 - \frac{\Delta R \times I_s}{I_s + \frac{I_0}{1 + Z^2/Z_0^2}}\right) \Big/ (1 - \Delta R) \tag{1}$$

where T stands for the normalized transmittance, I_0 is the incident pulse intensity, I_s denotes the saturation intensity, ΔR represents the modulation depth and the Z_0 represents the Rayleigh length. The above results manifest that the saturation absorption properties of Ag:SiO_2 at 1 μm waveband is efficiently modulated by embedded Ag NPs, and indicate that Ag:SiO_2 has great potential in Q-switched operation.

3. Ag:SiO_2-based Q-switched vortex waveguide laser

To comprehensively evaluate the performance of Ag:SiO_2 in Q-switched configuration, it is integrated into Nd:YAG "ear-like" single-cladding waveguide platform for Q-switched vortex laser. The schematic diagram of the experimental setup is shown in Fig. 5. The Nd:YAG "ear-like" single-cladding waveguide (prepared by using femtosecond laser direct writing technology to write additional track lines on both sides of the single-cladding waveguide track [50,51], the cross-section diagrams of the "ear-like" single-cladding waveguide and the single-cladding waveguide are shown in the inset of Fig. 5 respectively) with the diameter of 25 μm is used as the laser gain medium. A tunable CW Ti: Sapphire laser (Coherent MBR 110) with a central wavelength of 808 nm is utilized as pump source to excite the vortex laser with the wavelength of 1064 nm. A half-wave plate (optical transmittance > 98%) is employed to control the polarization state of the pump laser. A spherical planoconvex lens with $f = 30$ mm is used to couple the pump laser into the input end-face of the Nd:YAG waveguide. An input mirror (with the reflectivity of >99.9% at 1064 nm and the high transmittance of 99.75% at 808 nm), the Nd:YAG waveguide, and a spiral phase plate (topological

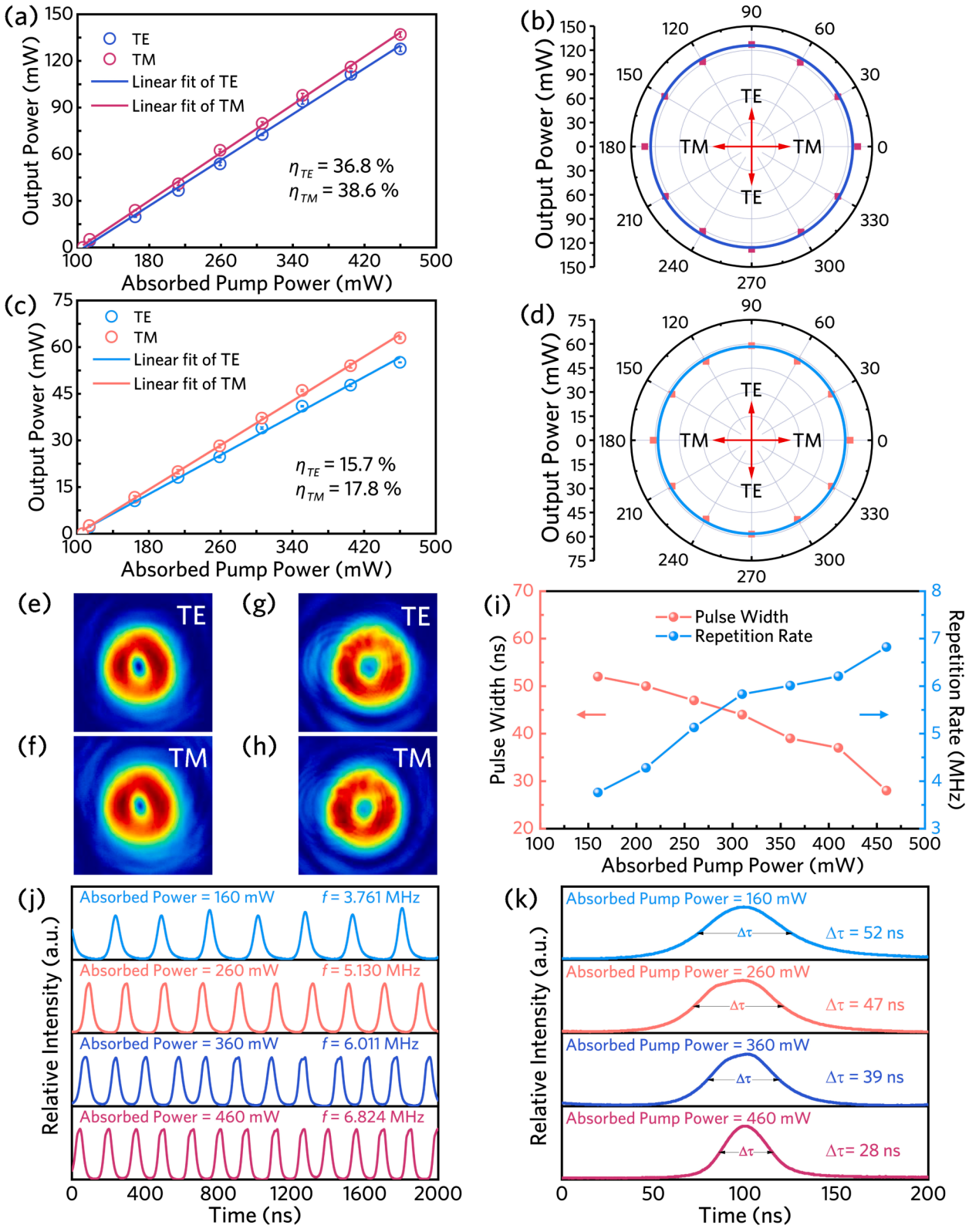

Fig. 6. (a) The output power of the CW vortex laser as a function of absorbed pump power under TE and TM polarizations. The error bars within the symbols of the data points represent the range of power fluctuations (b) The output power of the CW vortex laser for all-angle polarization. The modal profiles of the CW vortex laser under TE (e) and TM (f) polarizations. (c) The output power of the Q-switched vortex laser as a function of absorbed pump power under TE and TM polarizations. The error bars within the symbols of the data points represent the range of power fluctuations (d) The output power of the Q-switched vortex laser for all-angle polarization. The modal profiles of the Q-switched vortex laser under TE (g) and TM (h) polarizations. (i) Pulse width and repetition rate versus the absorbed pump power. (j) Recorded the pulse train of the Q-switched vortex laser. (k) Recorded the monopulse of the Q-switched vortex laser.

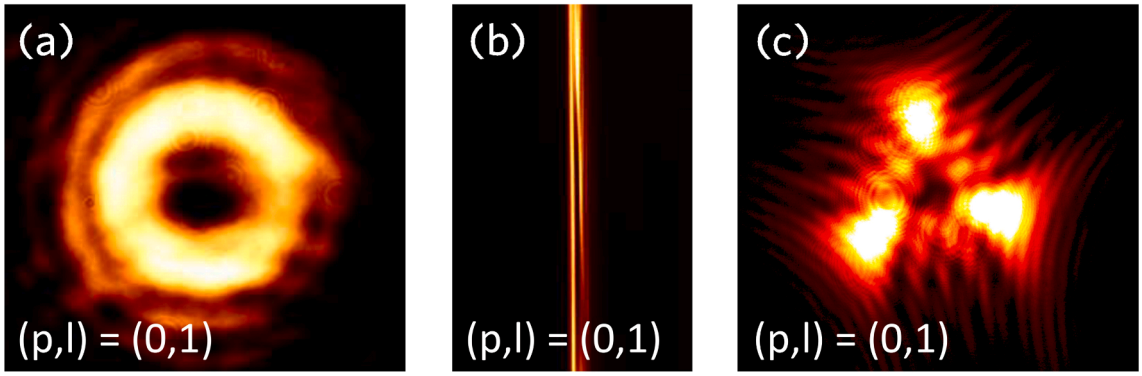

Fig. 7. Determination of the topological charge number. (a) The intensity profile of far-field output vortex beam. (b) The intensity profile of vortex beam obtained by focusing beam with the cylindrical lens. (c) The intensity profile of vortex beam obtained by diffraction through an equilateral triangular aperture. *p* represents the radial index; *l* represents the angular exponent, which is the topological charge of the vortex beam.

charge: 1; operating wavelength: 1030 nm; optical transmittance > 99%; center wavelength bandwidth: ± 35 nm; clear aperture: 4 mm) make up the waveguide vortex laser cavity. The spiral phase plate not only serves as an output mirror to provide optical feedback but also acts as a phase modulation element to transform the fundamental mode Gaussian beam into the LG beam in the cavity. Output laser is coupled by a 20 × microscope objective (NA = 0.40), and the pump laser remained is filtered by a long-pass filter. The power of the output laser is measured by an integrating sphere photodiode power sensor (Thorlabs, S145C), and the spot characteristics are collected by a CCD (Charge-coupled Device).

Initially, the performance of the CW Nd:YAG laser with a flat mirror as the output coupler is measured to evaluate the waveguide properties. Under TM polarization, the CW laser shows a maximum output power of 137 mW with a slope efficiency of 38.6%. Under TE polarization, the maximum output power is 128 mW with a slope efficiency of 36.8%, as shown in Fig. 6(a). By adjusting the half-wave plate, output power under full-angle polarization is measured and shown in Fig. 6(b). The fitting curve is approximately circular, indicating that the output power of the laser is not affected by polarization. This is because the Nd:YAG crystal used in the laser is a garnet crystal, belonging to the equiaxial crystal system, where the optical properties in the π and σ directions are essentially the same. The laser spots collected by CCD under TE and TM polarizations both exhibit an obvious doughnut shape, as shown in Fig. 6 (e) and 6(f), which is a characteristic sign of a vortex beam.

By inserting the Ag:SiO_2 SA into the cavity, the Q-switched vortex laser has been successfully realized. Nevertheless, the insertion of SA introduces some insertion loss, leading to an increase in the laser threshold. Compared to the CW laser, the output power of the Q-switched pulse laser experiences a notable reduction, as shown in Fig. 6 (c) and 6(d). And the Q-switched laser spots under TE and TM polarizations both are shown in Fig. 6(g) and 6(h), respectively. The variation trends of the pulse width and the repetition rate of Q-switched vortex laser as the absorbed pump power are depicted in Fig. 6(i), it can be summarized that the pulse width decreases from 52 ns to 28 ns with the absorbed pump power increasing, simultaneously, the repetition rate is tunable ranging from 3.761 MHz to 6.824 MHz. The pulse train and the monopulse of the Q-switched laser are recorded in Fig. 6(j) and 6(k), respectively. We believe the 28 ns pulse to be the shortest one ever reported for the Nd:YAG waveguide platform to realize Q-switched vortex laser. The stable nanosecond and megahertz Q-switched vortex laser further confirms that Ag:SiO_2 possess excellent saturation absorption characteristics and can achieve Q-switched operation in the near infrared band. Significantly, the Q-switched vortex laser show an excellent environmental stability, because the Ag NPs are buried inside SiO_2 dielectric material and not easily oxidized.

To further characterize the OAM carried by the vortex laser realized on the waveguide platform, the methods of cylindrical lens focusing and equilateral triangular aperture diffraction are employed to ascertain the topological charge of the beam. The intensity profile of the vortex laser collected in the Q-switched laser experimental setup is displayed in Fig. 7(a), which is in the shape of a doughnut. A cylindrical lens is placed behind the filter, and the vortex beam with topological charge of N is focused by the cylindrical lens and displays N + 1 optical bright lines [52]. Fig. 7(b) illustrates the intensity profile of the laser collected at the focal position of the cylindrical lens, from which two clear optical bright lines can be seen. And the focused spot follows the direction of the antidiagonal, indicating that the topological charge number is +1. In addition, the equilateral triangular aperture diffraction method is also used to verify the topological charge of the vortex beam. An equilateral triangular aperture is placed in front of the CCD, the vortex beam with topological charge of N diffracted through the aperture presents a triangular Fraunhofer diffraction pattern, and the number of spots along one edge of the triangle is N + 1 [53]. The intensity profile of the diffraction beam is depicted in Fig. 7(c), and the triangular diffraction pattern is rotated 30° counterclockwise with respect to the triangular aperture, again proving that the topological charge number is +1.

4. Conclusion

In summary, we report the linear and nonlinear optical absorption properties of Ag:SiO_2, and integrate it as an SA into an in-cavity phase modulated Nd:YAG waveguide platform to realize a Q-switched vortex laser at 1 μm band. It is proved that Ag:SiO_2 can be used as an SA to fabricate Q-switched vortex lasers with short pulse width and high repetition frequency. This work not only shows the significant potential of fused silica embedded with noble metallic NPs in Q-switched laser system, but also opens the way for the development of low-cost integrated photonic devices based on fused silica, further expands the broadband application of fused silica materials in various optical systems and devices.

CRediT authorship contribution statement

Wenqing Sun: Writing – original draft, Investigation, Formal analysis, Data curation. **Fengqin Liu:** Methodology, Investigation, Formal analysis. **Jing Guan:** Investigation, Formal analysis. **Carolina Romero:** Methodology, Investigation. **Javier R. Vázquez de Aldana:** Methodology, Investigation, Data curation. **Feng Ren:** Writing – review & editing, Conceptualization. **Yuechen Jia:** Writing – review & editing, Project administration, Methodology. **Xiaoli Sun:** Writing – review & editing, Investigation, Data curation, Conceptualization. **Feng Chen:** Writing – review & editing, Conceptualization.

Declaration of competing interest

The authors declare that they have no known competing financial interests or personal relationships that could have appeared to influence the work reported in this paper.

Data availability

Data will be made available on request.

Acknowledgments

This work was supported by the National Natural Science Foundation of China (12104256, 12235009,12074223), Natural Science Foundation of Shandong Province, China (ZR2021QA020, 2022HWYQ-047), and the Taishan Scholars Program of Shandong Province, China (tsqn201909041). X. L. Sun acknowledges the support from the "Young Scholars Program" of Shandong University, China.

References

[1] L. Allen, M.W. Beijersbergen, R.J.C. Spreeuw, J.P. Woerdman, Orbital angular momentum of light and the transformation of Laguerre-Gaussian laser modes, Phys. Rev. A 45 (1992) 8185–8189, https://doi.org/10.1103/PhysRevA.45.8185.
[2] Z.C. Zhang, L. Hai, S.Y. Fu, C.Q. Gao, Advances on solid-state vortex laser, Photonics 9 (2022) 215, https://doi.org/10.3390/photonics9040215.
[3] J.C. Ni, C. Huang, L.M. Zhou, M. Gu, Q.H. Song, Y.R. Kivshar, C.W. Qiu, Multidimensional phase singularities in nanophotonics, Science 374 (2021) eabj0039, https://doi.org/10.1126/science.abj0039.
[4] Y.J. Shen, X.J. Wang, Z.W. Xie, C.J. Min, X. Fu, Q. Liu, M.L. Gong, X.C. Yuan, Optical vortices 30 years on: OAM manipulation from topological charge to multiple singularities, Light Sci. Appl. 8 (2019) 90, https://doi.org/10.1038/s41377-019-0194-2.
[5] M. Padgett, R. Bowman, Tweezers with a twist, Nat. Photon. 5 (2011) 343–348, https://doi.org/10.1038/nphoton.2011.81.
[6] Y.J. Yang, Y.X. Ren, M.Z. Chen, Y. Arita, C. Rosales-Guzmán, Optical trapping with structured light: a review, Adv. Photon. 3 (2021), https://doi.org/10.1117/1.AP.3.3.034001.
[7] Y.Q. Zhang, J.F. Shen, C.J. Min, Y.F. Jin, Y.Q. Jiang, J. Liu, S.W. Zhu, Y.L. Sheng, A. V. Zayats, X.C. Yuan, Nonlinearity-induced multiplexed optical trapping and manipulation with femtosecond vector beams, Nano Lett. 18 (2018) 5538–5543, https://doi.org/10.1021/acs.nanolett.8b01929.
[8] L. Liu, Y.S. Gao, X.Z. Liu, High-dimensional vortex beam encoding/decoding for high-speed free-space optical communication, Opt. Commun. 452 (2019) 40–47, https://doi.org/10.1016/j.optcom.2019.06.061.
[9] C. He, Y.J. Shen, A. Forbes, Towards higher-dimensional structured light, Light Sci. Appl. 11 (2022) 205, https://doi.org/10.1038/s41377-022-00897-3.
[10] J. Leach, B. Jack, J. Romero, A.K. Jha, A.M. Yao, S. Franke-Arnold, D.G. Ireland, R. W. Boyd, S.M. Barnett, M.J. Padgett, Quantum correlations in optical angle-orbital angular momentum variables, Science 329 (2010) 662–665, https://doi.org/10.1126/science.1190523.
[11] D.S. Ding, W. Zhang, Z.Y. Zhou, S. Shi, G.Y. Xiang, X.S. Wang, Y.K. Jiang, B.S. Shi, G.C. Guo, Quantum storage of orbital angular momentum entanglement in an atomic ensemble, Phys. Rev. Lett. 114 (2015) 050502, https://doi.org/10.1103/PhysRevLett.114.050502.
[12] M. Duocastella, C.B. Arnold, Bessel and annular beams for materials processing, Laser Photonics Rev. 6 (2012) 607–621, https://doi.org/10.1002/lpor.201100031.
[13] O.J. Allegre, Y. Jin, W. Perrie, J. Ouyang, E. Fearon, S.P. Edwardson, G. Dearden, Complete wavefront and polarization control for ultrashort-pulse laser microprocessing, Opt. Express, OE 21 (2013) 21198–21207, https://doi.org/10.1364/OE.21.021198.
[14] J.Y. Wang, F.F. Li, G.G. Kang, Multiwavelength achromatic super-resolution focusing via a metasurface-empowered controlled generation of focused cylindrically polarized vortex beams, Opt. Express 30 (2022) 30811, https://doi.org/10.1364/OE.462900.
[15] C.L. Zhang, C.J. Min, L.P. Du, X.C. Yuan, Perfect optical vortex enhanced surface plasmon excitation for plasmonic structured illumination microscopy imaging, Appl. Phys. Lett. 108 (2016) 201601, https://doi.org/10.1063/1.4948249.
[16] S. Fürhapter, A. Jesacher, S. Bernet, M. Ritsch-Marte, Spiral phase contrast imaging in microscopy, Opt. Express 13 (2005) 689, https://doi.org/10.1364/OPEX.13.000689.
[17] M. Zürch, C. Kern, P. Hansinger, A. Dreischuh, Ch. Spielmann, Strong-field physics with singular light beams, Nature Phys. 8 (2012) 743–746, https://doi.org/10.1038/nphys2397.
[18] H. Sroor, Y.W. Huang, B. Sephton, D. Naidoo, A. Vallés, V. Ginis, C.W. Qiu, A. Ambrosio, F. Capasso, A. Forbes, High-purity orbital angular momentum states from a visible metasurface laser, Nat. Photon. 14 (2020) 498–503, https://doi.org/10.1038/s41566-020-0623-z.
[19] D. Naidoo, F.S. Roux, A. Dudley, I. Litvin, B. Piccirillo, L. Marrucci, A. Forbes, Controlled generation of higher-order Poincaré sphere beams from a laser, Nat. Photon. 10 (2016) 327–332, https://doi.org/10.1038/nphoton.2016.37.
[20] Y.J. Shen, X.L. Yang, D. Naidoo, X. Fu, A. Forbes, Structured ray-wave vector vortex beams in multiple degrees of freedom from a laser, Optica 7 (2020) 820, https://doi.org/10.1364/OPTICA.382994.
[21] R. Oron, Y. Danziger, N. Davidson, A.A. Friesem, E. Hasman, Laser mode discrimination with intra-cavity spiral phase elements, Opt. Commun. 169 (1999) 115–121, https://doi.org/10.1016/S0030-4018(99)00389-2.
[22] S. Ngcobo, I. Litvin, L. Burger, A. Forbes, A digital laser for on-demand laser modes, Nat. Commun. 4 (2013) 2289, https://doi.org/10.1038/ncomms3289.
[23] Y. Zhuang, S.X. Wang, Z.X. Chen, Y.C. Jia, W.G. Zhang, Y.C. Yao, Y.Y. Ren, F. Chen, H.L. Liu, Tailored vortex lasing based on hybrid waveguide-grating architecture in solid-state crystal, Appl. Phys. Lett. 120 (2022) 211101, https://doi.org/10.1063/5.0094288.
[24] L. Yang, D.D. Qian, C. Xin, Z.J. Hu, S.Y. Ji, D. Wu, Y.L. Hu, J.W. Li, W.H. Huang, J. R. Chu, Direct laser writing of complex microtubes using femtosecond vortex beams, Appl. Phys. Lett. 110 (2017) 221103, https://doi.org/10.1063/1.4984744.
[25] L.P. Gong, B. Gu, G.H. Rui, Y.P. Cui, Z.Q. Zhu, Q.W. Zhan, Optical forces of focused femtosecond laser pulses on nonlinear optical Rayleigh particles, Photon. Res. 6 (2018) 138, https://doi.org/10.1364/PRJ.6.000138.
[26] F.Q. Kong, C.M. Zhang, F. Bouchard, Z.Y. Li, G.G. Brown, D.H. Ko, T.J. Hammond, L. Arissian, R.W. Boyd, E. Karimi, P.B. Corkum, Controlling the orbital angular momentum of high harmonic vortices, Nat. Commun. 8 (2017) 14970, https://doi.org/10.1038/ncomms14970.
[27] Y.G. Zhao, Z.P. Wang, H.H. Yu, S.D. Zhuang, H.J. Zhang, X.D. Xu, J. Xu, X.G. Xu, J. Y. Wang, Direct generation of optical vortex pulses, Appl. Phys. Lett. 101 (2012) 031113, https://doi.org/10.1063/1.4737943.
[28] Q.Y. Tian, B. Xu, N. Li, Z.Q. Luo, H.Y. Xu, Z.P. Cai, Direct generation of orthogonally polarized dual-wavelength continuous-wave and passively Q-switched vortex beam in diode-pumped Pr:YLF lasers, Opt. Lett. 44 (2019) 5586, https://doi.org/10.1364/OL.44.005586.
[29] H.S. He, Z. Chen, H.B. Li, J. Dong, Low-threshold, nanosecond, high-repetition-rate vortex pulses with controllable helicity generated in Cr, Nd:YAG self-Q-switched microchip laser, Laser Phys. 28 (2018) 055802, https://doi.org/10.1088/1555-6611/aaad4c.
[30] Y.X. Bian, Z.N. Wang, Vortex random lasing with tunable wavelength and orbital angular momentum, Appl. Phys. Lett. 124 (2024) 073301, https://doi.org/10.1063/5.0189135.
[31] R. Woodward, E. Kelleher, 2D Saturable absorbers for fibre lasers, Appl. Sci. 5 (2015) 1440–1456, https://doi.org/10.3390/app5041440.
[32] X.F. Liu, Q.B. Guo, J.R. Qiu, Emerging low-dimensional materials for nonlinear optics and ultrafast photonics, Adv. Mater. 29 (2017) 1605886, https://doi.org/10.1002/adma.201605886.
[33] Y. Tan, Z.N. Guo, L.N. Ma, H. Zhang, S. Akhmadaliev, S.Q. Zhou, F. Chen, Q-switched waveguide laser based on two-dimensional semiconducting materials: tungsten disulfide and black phosphorous, Opt. Express 24 (2016) 2858–2866, https://doi.org/10.1364/OE.24.002858.
[34] S.X. Wang, X.L. Sun, H.L. Liu, Y.Y. Ren, Y.C. Jia, F. Chen, Femtosecond laser direct writing of Nd:YLF cladding waveguides for efficient 1047-nm laser emission, Opt. Mater. Express 11 (2021) 2915, https://doi.org/10.1364/OME.435194.
[35] R. Li, C. Pang, Z.Q. Li, M. Yang, H. Amekura, N.N. Dong, J. Wang, F. Ren, Q. Wu, F. Chen, Fused silica with embedded 2D-like Ag nanoparticle monolayer: tunable saturable absorbers by interparticle spacing manipulation, Laser Photonics Rev. 14 (2020) 1900302, https://doi.org/10.1002/lpor.201900302.
[36] C. Pang, R. Li, Z.Q. Li, N.N. Dong, C. Cheng, W.J. Nie, R. Böttger, S.Q. Zhou, J. Wang, F. Chen, Lithium niobate crystal with embedded au nanoparticles: a new saturable absorber for efficient mode-locking of ultrafast laser pulses at 1 μm, Adv. Opt. Mater. 6 (2018) 1800357, https://doi.org/10.1002/adom.201800357.
[37] X.L. Sun, L. Chu, F. Ren, Y.C. Jia, F. Chen, Plasmon-enhanced third-order optical nonlinearity of monolayer MoS2, Appl. Phys. Lett. 120 (2022) 193101, https://doi.org/10.1063/5.0091855.
[38] D. Ila, E.K. Williams, S. Sarkisov, C.C. Smith, D.B. Poker, D.K. Hensley, Formation of metallic nanoclusters in silica by ion implantation, Nucl. Instrum. Methods Phys. Res. B 141 (1998) 289–293, https://doi.org/10.1016/S0168-583X(98)00072-X.
[39] Y.X. Zhang, Y.H. Wang, Nonlinear optical properties of metal nanoparticles: a review, RSC Adv. 7 (2017) 45129–45144, https://doi.org/10.1039/C7RA07551K.
[40] R. Li, C. Pang, Z.Q. Li, F. Chen, Plasmonic nanoparticles in dielectrics synthesized by ion beams: optical properties and photonic applications, Adv. Opt. Mater. 8 (2020) 1902087, https://doi.org/10.1002/adom.201902087.
[41] L. Thylén, L. Wosinski, Integrated photonics in the 21st century, Photon. Res., PRJ 2 (2014) 75–81. Doi: 10.1364/PRJ.2.000075.
[42] Y. Meng, Y.Z. Chen, L.H. Lu, Y.M. Ding, A. Cusano, J.A. Fan, Q.M. Hu, K.Y. Wang, Z.W. Xie, Z.T. Liu, Y.M. Yang, Q. Liu, M.L. Gong, Q.R. Xiao, S.L. Sun, M.M. Zhang, X.C. Yuan, X.J. Ni, Optical meta-waveguides for integrated photonics and beyond, Light Sci. Appl. 10 (2021) 235, https://doi.org/10.1038/s41377-021-00655-x.
[43] F. Chen, J.R.V. de Aldana, Optical waveguides in crystalline dielectric materials produced by femtosecond-laser micromachining, Laser Photonics Rev. 8 (2014) 251–275, https://doi.org/10.1002/lpor.201300025.
[44] C. Guerra-Olvera, G.R. Castillo, E.H. Penilla, G. Uahengo, J.E. Garay, S. Camacho-Lopez, Circular depressed cladding waveguides in mechanically robust, biocompatible nc-YSZ transparent ceramics by fs laser pulses, J. Lightwave Technol. 37 (2019) 3119–3126, https://doi.org/10.1109/JLT.2019.2911256.
[45] Y.C. Jia, S.X. Wang, F. Chen, Femtosecond laser direct writing of flexibly configured waveguide geometries in optical crystals: fabrication and application,

Opto-Electron. Adv. 3 (2020) 190042, https://doi.org/10.29026/oea.2020.190042.
[46] G.W. Arnold, J.A. Borders, Aggregation and migration of ion-implanted silver in lithia-alumina-silica glass, J. Appl. Phys. 48 (1977) 1488–1496, https://doi.org/10.1063/1.323867.
[47] N. Matsunami, H. Hosono, Colloid formation effects on depth profile of implanted Ag in SiO_2 glass, Appl. Phys. Lett. 63 (1993) 2050–2052, https://doi.org/10.1063/1.110588.
[48] B. Can-Uc, R. Rangel-Rojo, L. Rodriguez-Fernandez, A. Oliver, Polarization selectable nonlinearities in elongated silver nanoparticles embedded in silica, Opt. Mater. Express, OME 3 (2013) 2012–2021, https://doi.org/10.1364/OME.3.002012.
[49] A. Berger, K.-J. Berg, H. Hofmeister, Aggregates of small silver particles in surface layers of glasses — electron microscopy and optical microspectroscopy, Z Phys. D - Atoms, Molecules Clusters 20 (1991) 313–315, https://doi.org/10.1007/BF01543999.
[50] A. Okhrimchuk, V. Mezentsev, A. Shestakov, I. Bennion, Low loss depressed cladding waveguide inscribed in YAG: Nd single crystal by femtosecond laser pulses, Opt. Express 20 (2012) 3832, https://doi.org/10.1364/OE.20.003832.
[51] X.L. Sun, S. Sun, C. Romero, J.R. Vázquez de Aldana, F.Q. Liu, Y.C. Jia, F. Chen, Femtosecond laser direct writing of depressed cladding waveguides in Nd:YAG with “ear-like” structures: fabrication and laser generation, Opt. Express 29 (2021) 4296, https://doi.org/10.1364/OE.417815.
[52] S.N. Alperin, R.D. Niederriter, J.T. Gopinath, M.E. Siemens, Quantitative measurement of the orbital angular momentum of light with a single, stationary lens, Opt. Lett., OL 41 (2016) 5019–5022, https://doi.org/10.1364/OL.41.005019.
[53] J.M. Hickmann, E.J.S. Fonseca, W.C. Soares, S. Chávez-Cerda, Unveiling a truncated optical lattice associated with a triangular aperture using light’s orbital angular momentum, Phys. Rev. Lett. 105 (2010) 053904, https://doi.org/10.1103/PhysRevLett.105.053904.